JOURNAL OF SYNCHROTRON RADIATION

ISSN 1600-5775

Characterization of enamel caries lesions in rat molars using synchrotron X-ray microtomography

R. D. Free,[a]* K. DeRocher,[a] S. R. Stock,[b] D. Keane,[a] K. Scott-Anne,[c] W. H. Bowen[c] and D. Joester[a]

[a]Department of Materials Science and Engineering, Northwestern University, Evanston, IL, USA, [b]Feinberg School of Medicine, Northwestern University, Chicago, IL, USA, and [c]Center for Oral Biology, University of Rochester, Rochester, NY, USA. *Correspondence e-mail: rfree@u.northwestern.edu

Received 31 March 2017
Accepted 12 June 2017

Edited by V. Favre-Nicolin, CEA and Université Joseph Fourier, France

Keywords: X-ray microtomography; white spot enamel lesions; surface zones; caries.

Dental caries is a ubiquitous infectious disease with a nearly 100% lifetime prevalence. Rodent caries models are widely used to investigate the etiology, progression and potential prevention or treatment of the disease. To explore the suitability of these models for deeper investigations of intact surface zones during enamel caries, the structures of early-stage carious lesions in rats were characterized and compared with previous reports on white spot enamel lesions in humans. Synchrotron X-ray microcomputed tomography non-destructively mapped demineralization in carious rat molar specimens across a range of caries severity, identifying 52 lesions across the 30 teeth imaged. Of these lesions, 13 were shown to have intact surface zones. Depth profiles of fractional mineral density were qualitatively similar to lesions in human teeth. However, the thickness of the surface zone in the rat model ranges from 10 to 58 μm, and is therefore significantly thinner than in human enamel. These results indicate that a fraction of lesions in rat caries possess an intact surface zone and are qualitatively similar to human lesions at the micrometer scale. This suggests that rat caries models may be a suitable analog through which to investigate the structure of surface zone enamel and its role during dental caries.

1. Introduction

Dental caries, or tooth decay, is an infectious disease that has affected, or will affect, nearly every individual at some point (WHO, 2012). The disease begins when demineralization of enamel by bacteria-produced acids can no longer be counteracted by remineralization from saliva, leading to a net loss of mineral (Robinson *et al.*, 2000). While relatively innocuous in its earliest stages, once the disease progresses through the enamel it can cause severe pain and lead to tooth loss, systemic infection and possibly death. Furthermore, a myriad of negative secondary effects are associated with compromised oral health, including decline in overall physical and mental health, social isolation, and economic losses at an individual and societal level (HHS, 2000). Increased oral fluoride concentrations and improved oral hygiene education have significantly reduced the impact of caries for many Americans over the past half-century (CDC, 1999), but those from socioeconomically marginalized groups still suffer disproportionately. Additionally, since the early 2000s, the prevalence of early childhood caries has once again begun to increase (Kawashita *et al.*, 2011), suggesting a regression in the progress to combat the disease. For these reasons, the ability to diagnose, treat and prevent caries at an early stage has been, and will continue to be, a significant public health focus.

Much of our current knowledge of early-stage caries is based on characterization of so-called white spot enamel

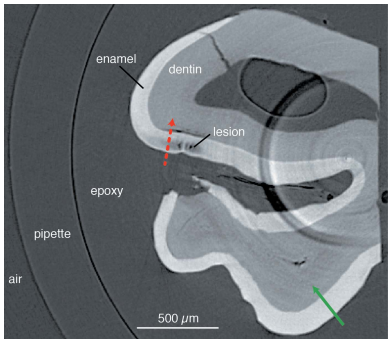

lesions (WSELs) in human enamel. WSELs form over time when demineralization outpaces remineralization, and they are the first clinically apparent sign of caries (Nanci, 2012). They consist of four distinct zones as defined by polarized light studies (Robinson *et al.*, 2000; Poole *et al.*, 1961). Of specific interest is the outermost intact surface zone (SZ) that appears to remain highly mineralized throughout the early development of the lesion. SZs have been observed in human WSELs by numerous techniques, including optical microscopy polarized light, scanning X-ray microradiography, X-ray microcomputed tomography (μCT) and optical coherence tomography (Wefel & Harless, 1984; Elliott *et al.*, 1981; Huang *et al.*, 2007; Eanes, 1979). They have also been generated *in vitro* using low pH, cycling pH or fluoridating the demineralization solutions (Margolis *et al.*, 1999; Yamazaki & Margolis, 2008; Yamazaki *et al.*, 2007). Arends & Christoffersen (1986) have reviewed the many proposed mechanisms and models for SZ formation during both *in vivo* and *in vitro* lesion formation. However, the complexity of the system and dynamic nature of the dissolution/remineralization processes have prevented a definitive explanation of why and how the SZ forms. Furthermore, little is known about the evolution of enamel before the WSEL is fully established, and, while the mineral density of the SZ is comparable with sound enamel, it is unclear to what degree the structure and chemistry have been affected by the lesion development. Because it is the outermost diffusive barrier that presumably mediates ongoing demineralization and ion transport processes, a better understanding of the structure and evolution of the SZ is vital to understanding the dynamics of early caries development.

Rodent caries models have long served as an *in vivo* proxy to investigate the human disease and have produced much of the current knowledge of disease pathology and treatment. This includes demonstrating the importance of diet (Kite *et al.*, 1950), uncovering the impact of eating frequency on caries induction (König *et al.*, 1968), establishing the necessity of bacterial involvement and infectious nature of the disease (Orland *et al.*, 1955; Keyes, 1960), and revealing the preventative effect of topically applied fluoride (Cheyne, 1940). Today, such models are frequently used to explore the cariogenicity of different diets and test the efficacy of oral hygiene products (Bowen, 2013). These models provide an *in vivo* system that can yield carious lesions within as few as two weeks and allow systematic control of dietary and biological factors. Although models have been widely used to evaluate the etiological factors of the disease, nearly all characterization of carious lesion microstructure and composition has been performed on lesions occurring in human enamel. Little is known about the actual structure of the induced lesions in rats at the microscale, and it is unclear how similar or different they may be from human lesions. For example, it is unclear whether induced carious lesions in rats possess SZs at all, one of the most important features of human WSELs.

In order to explore the viability of using a rodent caries model for detailed structural studies of carious lesions in general and SZs specifically, a non-destructive, quantitative imaging technique was desired. The application of both laboratory source and synchrotron absorption μCT to mineralized tissues is well established (Davis & Wong, 1996; Stock, 2008), and numerous studies have used the technique to explore the mineral density distribution in sound (Clementino-Luedemann & Kunzelmann, 2006; Dowker *et al.*, 2006) and carious human enamel (Dowker *et al.*, 2004; Clementino-Luedemann, 2007; Shahmoradi & Swain, 2017). Recently, the advent of advanced techniques, including small-angle X-ray scattering tomography (Schaff *et al.*, 2015), phase tomography (Zanette *et al.*, 2015; Gradl *et al.*, 2016) and microdiffraction (Al-Jawad *et al.*, 2007, 2012; Simmons *et al.*, 2013), has enabled mapping of structural parameters beyond mineral density. As our primary objective was to establish the existence and compare the gross structure of WSELs in murine enamel with those characterized previously by μCT in human enamel (Huang *et al.*, 2007, 2010; Cochrane *et al.*, 2012), we opted for the same technique. Significantly, we confirm the existence of intact SZs in rat caries and provide an overview of SZ lesion structure relative to human WSELs.

2. Materials and methods

2.1. Tooth specimens

Lesions in rat molars from three animals were generated using a desalivated caries model as part of a previous study (Bowen *et al.*, 1997). Caries severity was evaluated by the modified Keyes method (Keyes, 1958; Larson, 1981), yielding a semi-quantitative score of caries severity and the degree of demineralization for each tooth. Molars were hemisectioned and coated in nail varnish as part of this scoring method, then stored dry in 10 ml vials. Based on the Keyes scores, the three animals were identified to have limited/no caries, onset caries and progressed caries, respectively. A total of 30 specimens across these three groups were examined *via* μCT, primarily focusing on teeth from the limited/no caries and onset caries groups to target early stage lesions. The specimens were sampled from across the oral cavity, including teeth of all three molar types (Fig. 1) and from all four quadrants of the mouth (Table 1).

2.2. X-ray microtomography

2.2.1. Sample preparation. Individual teeth were isolated from hemisectioned (Fig. 1) maxillary and mandibular half-arcades by applying increasing pressure to the jawbone between teeth with a #10 scalpel until fracture. Forceps were used to stabilize the arcade during this process, and care was taken to avoid any direct manipulation or pressure on enamel surfaces. Isolated tooth hemisections were then either imaged without further manipulation or soaked in acetone for 30 s to remove the thin layer of nail varnish applied as part of the Keyes scoring. All samples were stored dry in 1 ml centrifuge tubes until mounting for X-ray microtomography.

2.2.2. Sample mounting. Sample mounts were prepared from 1 ml pipette tips. A razor blade was used to cut the pipette tips approximately 2 cm from the dispensing end. This yielded conical shells in which individual teeth could be gently

Table 1
Tooth specimens and distribution across the oral cavity.

Caries severity	Limited	Onset	Progressed
Nutrition†	Distilled water	Infant formula	5% sucrose water
Sample count	12	16	2
Distribution			
M1–M2–M3 molars	5–4–3	8–0–8	2–0–0
Maxillary mandibular	4–8	8–8	2–0
Buccal lingual	5–7	8–8	0–2
Right–left arcade	8–4	8–8	1–1

† See Bowen *et al.* (1997).

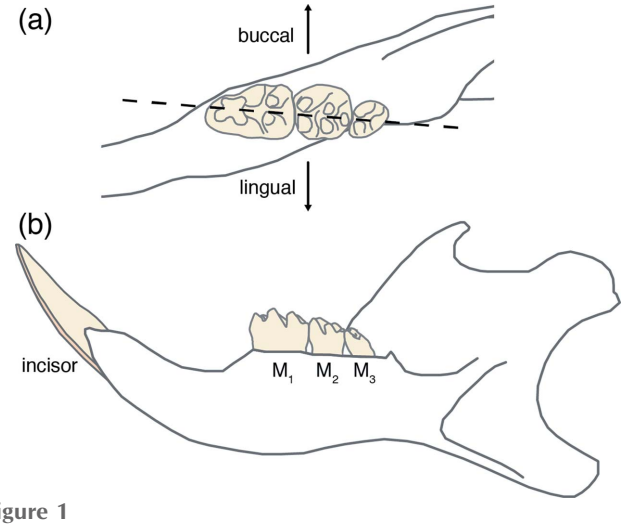

Figure 1
Schematic drawing of the right mandible of the rat. (*a*) Enlarged occlusal (top) aspect of the three molars M1, M2 and M3, and the mesio-distal plane (dotted line) along which hemisections were prepared for caries lesion scoring after Keyes (1958). (*b*) Lingual (tongue-facing) aspect of the whole mandible.

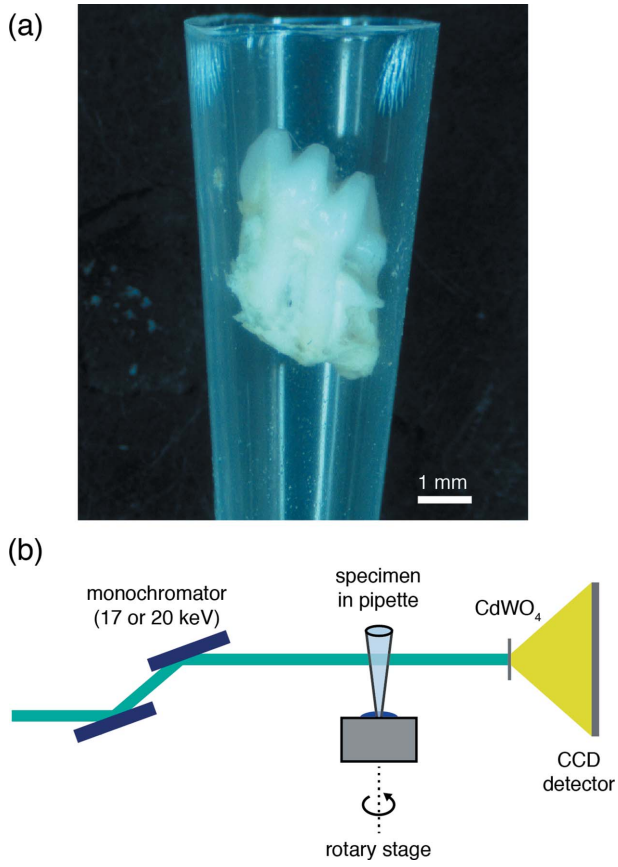

Figure 2
Sample mounting for synchrotron µCT. (*a*) The M1 molar wedged inside a modified pipette tip. (*b*) Schematic drawing of the experimental setup for data collection. A Si(111) double-crystal monochromator selects the beam energy. The specimen in the pipette tip is mounted on the rotation stage using a small piece of modelling clay. A cadmium tungstate ($CdWO_4$) single-crystal scintillator converts X-rays to an optical wavelength, which are then magnified by a 4× objective lens (numerical aperture of 0.2) and collected by CCD detector.

wedged and fixed rigidly (Fig. 2*a*). For those samples that had been soaked in acetone, the pipette tips were lastly infiltrated with Epo-fix 301 cold curing epoxy (Electron Microscopy Sciences, Hatfield, PA, USA) and cured at room temperature overnight.

2.2.3. Synchrotron µCT. Synchrotron µCT was performed on beamline 5-BM-C (DND-CAT) of the Advanced Photon Source (Argonne National Laboratory). This beamline was configured to perform tomography with a collimated, monochromatic beam to yield an isotropic voxel side length of 6 µm (Fig. 2*b*). For M1 and M2 molars, 20 keV monochromatic X-rays and a collection time of 800 ms maximized absorption contrast and utilized the full dynamic range of the detector. For the smaller M3 molars, the energy was reduced to 17 keV. Radiographs were collected with a 1300 × 1340, 24 µm pixel Roper scientific (Photometrics) CCD detector. Scans were performed with the beamline in top-up mode such that the X-ray flux was maintained over the course of an individual scan. Each scan consisted of 1200 projections over 180° (0.15° increments) and took approximately 2 h. At the beginning of each scan, a frame with the X-ray beam blocked (dark frame) was recorded to measure the detector noise. Every five projections, flat-field measurements with the sample removed from the beam path were collected to capture inhomogeneities inherent in the beam. These were used to normalize collected patterns and reduce noise through a conventional flat-field correction algorithm (Nieuwenhove *et al.*, 2015). Reconstructions were performed on site using a six-node Linux cluster implementing a filtered back-projection algorithm with a Shepp–Logan kernel. Intermediate reconstructions were viewed using the *IDL* software package (ITT Visual Information Solutions). Completed reconstructions consist of a three-dimensional dataset in a 16-bit ANALYZE data format that can be loaded into *ImageJ* (Schneider *et al.*, 2012) for further analysis.

2.3. Data analysis

2.3.1. Normalization. The dataset from each µCT scan consists of a three-dimensional matrix of linear attenuation coefficients (LACs), μ, corresponding to the average X-ray absorption within each voxel (volume pixel). For a region of uniform chemical composition, variations in μ can be attributed to variations in the material density (Stock, 2008). Thus,

because the compositional variations within enamel occur at length scales much smaller than the voxel size (6 µm), μ is assumed to be proportional to the enamel mineral density. Various approaches have been used to compute absolute mineral density in teeth from experimentally determined linear attenuation coefficients, including the use of aluminium standards (Clementino-Luedemann & Kunzelmann, 2006), calibration with hydroxyapatite phantoms of known density (Huang *et al.*, 2007; Djomehri *et al.*, 2015) and modelling enamel as a two-phase (mineral/organic) system (Dowker *et al.*, 2006). However, because μ varies with X-ray energy and enamel is inherently heterogeneous and multiphase, we chose here to instead compute a mineral volume fraction (f_m) based on the local LAC values for air and sound enamel as follows,

$$f_m = \frac{\mu_{meas} - \mu_{air}}{\mu_{enamel} - \mu_{air}} = \frac{V_m}{V}, \quad (1)$$

where μ_{meas} is the reconstructed LAC in the dataset, μ_{air} is the average LAC of air computed from an area within the central slice of the specific volume of interest, and μ_{enamel} is the average LAC for sound enamel taken from an area in the same slice that is clear of artifacts and demineralization. This approach (Fig. 3) yields a value for each voxel that corresponds to the volume of sound enamel mineral present (V_m) relative to the total volume of the voxel (V), *i.e.* the average phase fraction between pure air (f_m = 0) and sound enamel mineral (f_m = 1). Computation of the volume fraction of material from the LAC was first developed by Guvenilir and colleagues (Guvenilir *et al.*, 1997) to determine sub-voxel-sized crack openings. Since the density of enamel is ∼2000 times that of air, we can neglect the contribution of the latter and define a fractional mineral density (ρ^*) that is approximately equal to f_m,

$$\rho^* = \frac{\rho_{meas}}{\rho_{enamel}} \simeq f_m. \quad (2)$$

Multiplying the value of ρ^* by the average density of sound enamel will yield an approximate measure for the average mineral density within a given voxel. A similar normalization scheme for characterizing demineralization in human enamel has been previously reported by Lautensack and colleagues (Lautensack *et al.*, 2013).

2.3.2. Identifying lesions. Tomographic reconstructions were inspected for the presence of lesions by eye, slice by slice. We defined the following criteria to identify lesions: (i) the three-dimensional region must include at least 500 connected voxels (equivalent to 60 µm × 60 µm × 30 µm) with an average $\rho^* < 0.8$; (ii) the region must span at least five slices; and (iii) the region must be free from sharp ring artifacts that obscure the shape and ρ^* within the demineralized region [for an example, see Fig. 3(*a*)]. This conservative approach safeguards against false lesion identification near artifacts, but likely overlooks early-stage lesions with minimal demineralization.

2.3.3. Depth profiles. For regions of demineralization free from ring artifacts, *ImageJ* (Schneider *et al.*, 2012) was used to generate depth profiles of fractional mineral density (Fig. 3*c*).

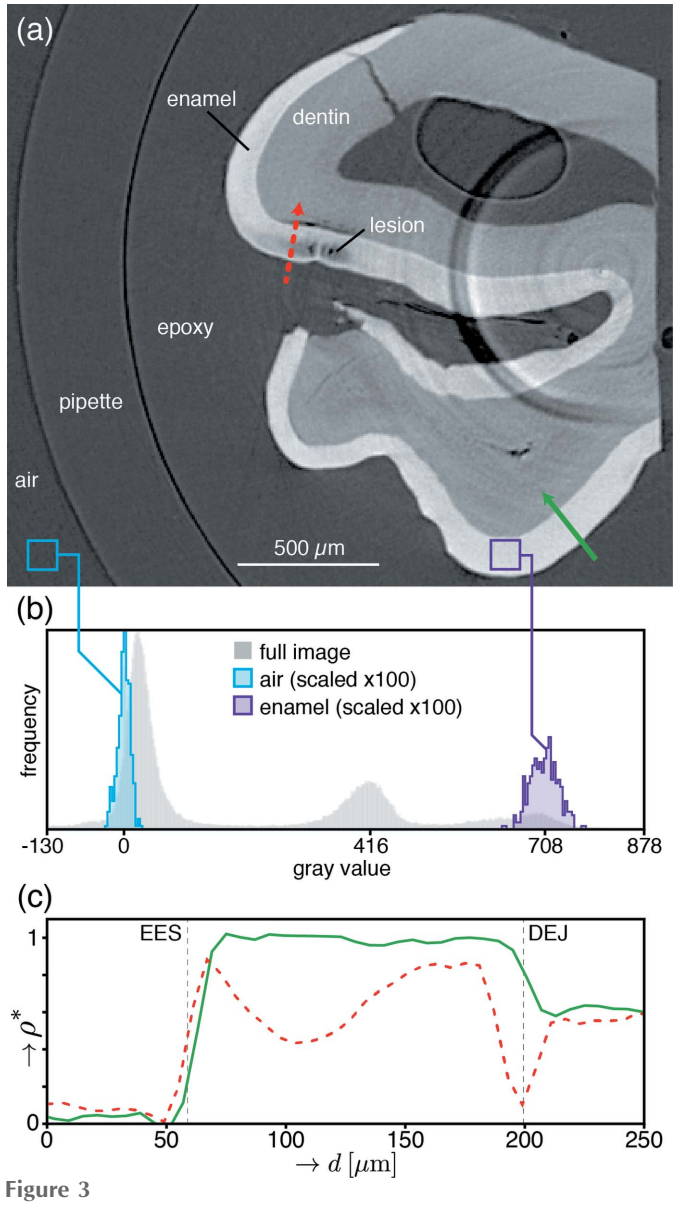

Figure 3
Example of data analysis workflow. (*a*) Representative slice containing regions of reduced absorption within enamel. Gray values correspond to linear attenuation coefficient (μ), with lighter shades representing greater X-ray absorption. The solid and dotted arrows correspond to the depth profiles in panel (*c*). (*b*) Histograms of gray values from the slice and subsample regions in panel (*a*). Contrast adjusted to span from −130 to 878 to capture meaningful features. The air (left) and enamel (right) subsample histograms were taken from the boxes shown in panel (*a*). The means of these subsamples are used to normalize the line profiles in panel (*c*) according to the procedure in §2.3.1. (*c*) Depth profiles of fractional mineral density (ρ^*) corresponding to the solid and dotted paths shown in panel (*a*). Generated according to the procedure outlined in §2.3.3.

Depth profiles were taken manually, oriented roughly normal to both the external enamel surface (EES) and dentino-enamel junction (DEJ). A line width of 3 voxels was used for each profile and profiles were collected along the same path from three consecutive slices. Thus, each point at a given depth in the profile consists of an average ρ^* across a volume that is 18 µm × 18 µm in cross section and 6 µm deep in the direction of the profile. For each lesion examined, three depth profiles

were taken through the demineralized region, and a similar profile through nearby sound enamel of comparable thickness was taken for reference. Because depth profiles are taken in the plane of the reconstructed slices, care must be taken to ensure that the surface normal of enamel analyzed *via* this procedure also lies in this plane. To facilitate this approach, tooth specimens were oriented during data collection such that the majority of enamel surfaces are properly oriented. Characterizing lesions where this is not the case requires either a rotation of the dataset or an alternative approach that accounts for the complete three-dimensional nature of the lesion.

2.3.4. Lesion classification. Lesions were classified based on features observed in the depth profiles [Figs. 4(*b*) and 4(*c*)]. Lesion severity was distinguished based on the minimum fractional mineral density, $\rho^*_{\rm min}$, observed within the lesion body (point D), with profiles displaying $\rho^*_{\rm min} < 0.5$ classified as severe and those with $\rho^*_{\rm min} > 0.5$ classified as mild. The presence of an intact SZ was also assessed for each identified lesion. To be classified as a SZ-containing lesion (SZL), ρ^* must be greater than $\rho^*_{\rm min}$ at some point exterior to the lesion body minimum [*e.g.* point B *versus* point D in Fig. 4(*c*)]. Furthermore, this condition must hold over a distance of at least 18 µm (3 voxels). This ensures that lesions are not mistakenly labelled as SZs due to artifacts present at the interface of weakly and strongly absorbing materials (*i.e.* the air–enamel interface). Importantly, SZLs must be entirely subsurface across their entire contiguous three-dimensional extent to be certain that demineralization has progressed through the external surface and not laterally through the enamel from an erosive lesion or compromised surface. Therefore, adjacent slices were carefully reviewed to ensure an intact surface for each putative SZL, and lesions intersecting with the cut surface of the tooth were dismissed from consideration to maintain a robust classification.

2.3.5. Surface zone lesion parameterization. For those lesions classified as SZLs, parameterization of the depth profiles was performed to quantify and compare the nature of demineralization (Fig. 4). Points along the profile were defined based on the computed values for ρ^*, and distances corresponding to SZ thickness, lesion depth and enamel thickness were subsequently calculated. The dimensionless quantity $\Delta_{\rm SZ}$ reflects the difference between the maximum and minimum value of ρ^* in the lesion, *i.e.* the normalized magnitude of over-mineralization of the SZ. The integrated demineralization ($m_{\rm L}$) represents the amount of mineral removed from the body of the lesion along the depth profile relative to sound enamel. It is qualitatively analogous to the 'integrated mineral lost', commonly represented as Δz, that is frequently reported in transverse microradiography studies of demineralization in thin enamel sections (Ten Bosch & Angmar-Månsson, 1991) and has been applied previously by Vieira and colleagues (Vieira *et al.*, 2006) using µCT. However, we would like to stress that $m_{\rm L}$ is computed in a slightly different manner than Δz and thus differs quantitatively. To better compare between SZLs, the lesion depth and integrated demineralization were both normalized. Specifically, the normalized depth of the

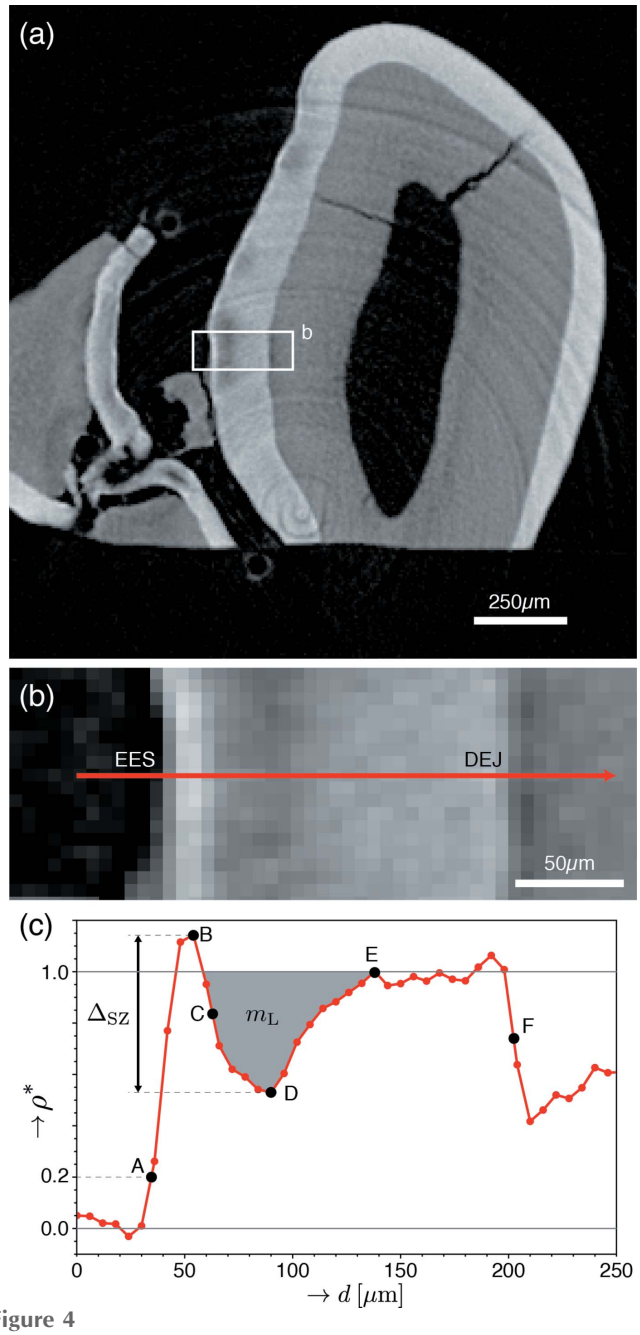

Figure 4
Definition of parameters used to characterize SZ lesions. (*a*) Contrast-adjusted slice containing mild lesions within the grooves between tooth cusps (sulcal surfaces). (*b*) Enlarged image of the boxed region in (*a*). (*c*) Plot of the fractional mineral density (ρ^*) against distance, taken along the red arrow in (*b*). Points used for profile quantification were defined as follows: external enamel surface (EES) (A), corresponding to $\rho^* = 0.2$; maximum (B), midpoint (C) and minimum (D) of ρ^* within the SZ and lesion; recovery to sound enamel ($\rho^* = 1$) (E); and DEJ (F). The midpoint (C) is defined as the depth at which ρ^* equals the average of that at points B and D. These points were selected following the approaches of Groeneveld & Arends (1975) and Cochrane *et al.* (2012) to facilitate direct comparison with human SZs. From these points, depth measurements were calculated for each lesion, including multiple representations for the SZ thickness (AB, AC and AD), total lesion depth (AE) and enamel thickness (AF). Furthermore, the SZ magnitude, $\Delta_{\rm SZ}$, was defined as the difference in ρ^* between points B and D. Finally, the integrated demineralization (shaded gray), $m_{\rm L}$, is defined as the integrated value of $1 - \rho^*$ (normalized mineral lost) within the body of the lesion (where $\rho^* < 1$).

lesion, d_L^*, is defined as the ratio between the lesion depth and total enamel thickness (*i.e.* AE/AF). The average normalized mineral lost, m_L^*, is defined as the ratio between the integrated demineralization and the expected value for sound enamel having the same thickness. Since sound enamel has $\rho^* = 1$, this amounts to dividing m_L by the distance between the bounds of integration used to compute m_L.

3. Results

3.1. Identification of carious lesions

Applying the procedure and classification criteria described in §2.3 to 30 tooth reconstructions, 52 total lesions were identified, including 13 that clearly display an intact SZ (summarized in Table 2). No demineralization was observed in any of the 12 molars from the limited/no caries group or any of the eight M3 molars taken from the onset caries group. The M1 molars from the onset caries group show the widest range of demineralization, including both mild and severe lesions, some of which possess intact SZs. The M1 specimens from the progressed caries group show the most significant demineralization, displaying only severe lesions with no intact SZs.

Obvious differences in the degree of demineralization were observed between teeth from the three experimental groups (representative examples in Fig. 5). The limited/no caries teeth [Figs. 5(*a*) and 5(*d*)] show intact enamel and dentin, with uniform μ observed within each tissue. The only deviations are associated with cracks in the tissue or imaging artifacts that may result from inhomogeneities in the X-ray beam, non-uniform detector element sensitivity, or non-linear scintillator response (Davis & Elliott, 2006). The M3 onset caries teeth are similarly free from regions of demineralization. In comparison, the M1 onset caries teeth [Figs. 5(*b*) and 5(*e*)] include regions within the enamel of localized demineralization. These contiguous regions of reduced μ are located near the enamel surface, but in some cases display a thin surface layer of higher-absorbing mineral constituting an intact SZ (Fig. 5*e*). Nearly all lesions from this stage are also associated with a separation at the DEJ beneath the lesion [asterisk (*) in Fig. 5*e*]. Finally, the progressed caries teeth [Figs. 5(*c*) and 5(*f*)] display significantly larger regions of demineralization, and an absence of intact SZs. Significant portions of both the enamel and dentin have been removed or compromised, and bands of higher and lower μ oriented normal to the DEJ and EES suggest some form of lesion substructure.

3.2. Surface zones in rodent caries

Of the 52 lesions classified, 13 show definitive SZs according to the conservative criteria described in §2.3.4. All of the SZLs were observed in M1 molars from the onset caries control group (see Table 2), six associated with mild lesions and seven with severe lesions. They occur in all four M1 molars and on both lingual- and buccal-facing hemisections. Examples of single slices containing SZLs are included in Figs. 3(*a*), 4, 5(*b*) and 5(*e*). In these illustrative examples, and indeed across the entire dataset, SZLs are observed primarily in the sulcal regions of the M1 molars. Seven of the identified SZLs were found in a single tooth reconstruction, the right maxillary buccal M1.

Key parameters were extracted from depth profiles for the 13 identified SZLs (Table 3). Following the approach of

Table 2
Summary of demineralization characterized with μCT.

Experimental group	Samples	No. of lesions characterized	
		Mild (w/SZ)†	Severe (w/SZ)†
Limited/no caries	Molar of mixed type (12)	0	0
Onset caries	M3 Molars (8)	0	0
	R mandibular buccal M1	4	0
	L mandibular lingual M1	5	0
	R maxillary lingual M1	4	0
	L maxillary lingual M1	6 (1)	0
	R maxillary buccal M1	8 (4)	3 (3)
	L mandibular buccal M1	2 (1)	1 (1)
	L maxillary buccal M1	1	2 (2)
	R mandibular lingual M1	5	1 (1)
Progressed caries	L maxillary lingual M1	0	4
	R maxillary lingual M1	0	6

† No. also containing intact SZ.

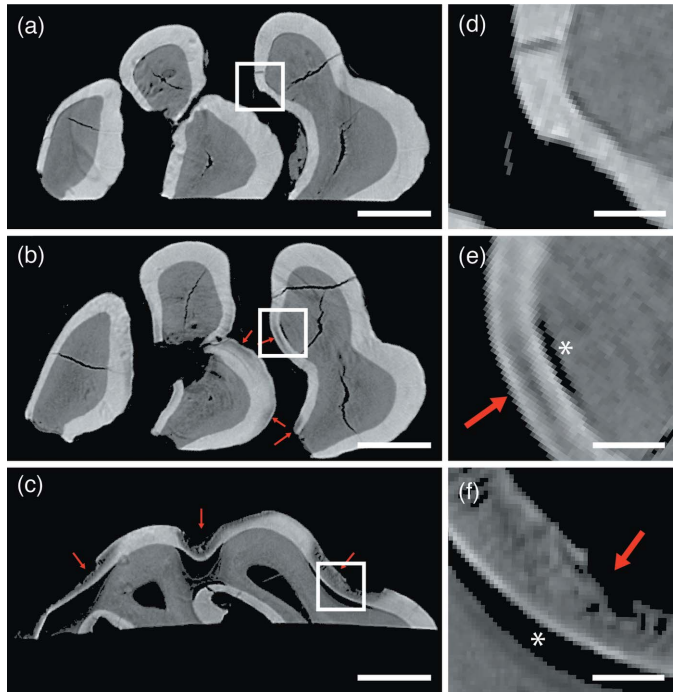

Figure 5
Examples of μCT reconstructions compared across experimental groups. Slices from comparable regions of the left, maxillary, lingual M1 molar from each of the (*a*) limited/no caries, (*b*) onset caries and (*c*) progressed caries experimental groups. Arrows indicate regions of demineralization. Images have been thresholded at a gray value of 200 such that regions of air appear black [see Fig. 3(*b*)]. Scale bars represent 500 μm. (*d*)–(*f*) Enlarged regions corresponding to the boxed regions in panels (*a*)–(*c*), respectively. The asterisks (*) indicate regions of DEJ separation. Scale bars represent 100 μm.

Table 3
Summary of parameters from characterized SZs.

Parameters†	Rat SZ lesions (n = 13)	Range	Human WSELs‡ (n = 8)
Thickness (μm)			
AB	13 ± 3	10–21	54.4 ± 17.8
AC	24 ± 5	17–32	126.9 ± 41.9
AD	42 ± 10	30–58	289.4 ± 145.8
AE	81 ± 21	60–113	525.6 ±198.7§
AF	99 ± 35	67–159	–
d_L^* (AE/AF)	0.85 ± 0.12	0.55–1.00	–
Δ_{SZ}	0.39 ± 0.13	0.18–0.52	–
m_L^*	29% ± 8%	15–43%	–

† Thickness measurements extracted from depth profiles as described in §2.3.5 and Fig. 3. ‡ Values for inactive human WSELs reproduced from Cochrane *et al.* (2012). § AE in this study corresponds to the thickness labeled AF in Cochrane *et al.* (2012).

Cochrane *et al.* (2012), multiple representations for the SZ thickness have been determined as described in §2.3.5 (Fig. 3). The surface-to-maximum (AB) distances range from 10 to 21 μm, surface-to-midpoint distances (AC) range from 17 to 32 μm, and surface-to-minimum distances (AD) range from 30 to 58 μm. The majority of lesions extend almost entirely through the enamel thickness to the DEJ, with 11 of the 13 SZLs characterized possessing a normalized lesion depth between 0.80 and 1.00. Surface zone magnitude values range from 0.18 to 0.52, with a mean of 0.39. The average normalized mineral lost ranges from 15% to 43%, with a mean of 29%.

4. Discussion

The qualitative extent and severity of demineralization characterized by a review of μCT reconstructions agrees well with the Keyes scores and cariogenicity of the various diets provided to each experimental group (Bowen *et al.*, 1997). The limited/no caries specimen group shows no discernable lesions, as expected based on the optical review. The variation in lesion severity between molar types within the onset caries group can be understood in terms of the factors promoting cariogenesis and the timeline of the study from which the teeth were acquired. The M3 molars, none of which show lesions (Table 2), erupt into the oral cavity last (age 35–40 days). As this study was terminated at age 42 days, M3 molars were exposed to cariogenic conditions between 2 and 7 days only. Furthermore, M3 molars have minimal sulcal surfaces in which plaque formation can easily proceed (Lyngstadaas *et al.*, 1998). Thus, these teeth experience the shortest period of cariogenic challenge and present primarily smooth surfaces on which biofilms can be easily disrupted during feeding or gnawing. Meanwhile, the M1 molars erupt earliest (at 19 days of age) and possess many obstructed sulcal surfaces that provide ideal conditions for plaque formation. Nearly all observed lesions in the M1 specimens from the onset caries group are located in these regions. Finally, the most severe demineralization is observed in the progressed caries group, in agreement with the high Keyes scores attributed to these samples.

The occurrence of SZLs within specific experimental groups suggests that induced rat caries progresses in a similar manner to natural human caries. In humans, WSELs constitute the first clinically observable disease state and possess intact SZs. The disease progresses in this state, with mineral being removed from the subsurface lesion body until the tissue is mechanically compromised and the SZ collapses (Robinson *et al.*, 2000). The observations that SZLs occur only in the onset caries group and that the progressed caries group includes only severe open lesions suggest that rodent caries may follow a similar progression. However, a larger study with tighter control over lesion development time is necessary to establish firm statistical support for this hypothesis.

The literature provides many approaches for quantifying SZ thicknesses in human WSELs, but a widely accepted definition has yet to emerge. In order to make direct comparisons between SZs in rodents and humans, three measurement methods have been applied here following Cochrane *et al.*'s (2012) analysis of WSELs in human caries imaged with μCT. In order of increasing thickness, these include the surface-to-maximum (AB) distance first employed by Groeneveld & Arends (1975), the surface-to-midpoint (AC) distance, and the surface-to-minimum (AD) distance (Fig. 4*c*). A fourth measurement approach outlined by Theuns *et al.* (1984) has been omitted here for clarity, but is implemented and discussed by Cochrane *et al.* (2012). Across 12 human carious lesions, Cochrane *et al.* report a range of AB distances from 35 to 130 μm, a range of AC distances from 55 to 190 μm, and a range of AD distances from 70 to 265 μm. Huang *et al.* (2007) also present μCT evidence of natural human WSELs with SZs consistent with these ranges. Here, the SZ thicknesses observed in rat lesions fall entirely below these ranges for each of the three measurement approaches: ranging from 10 to 21 μm, 17 to 32 μm, 30 to 58 μm, respectively. Clearly, SZs in rodents are significantly thinner than those observed in human caries lesions.

Cochrane *et al.* (2012) suggest that the AB distance used as an indicator of SZ thickness by Groeneveld & Arends (1975) be used to compare measurements between studies to maintain consistency. While the AB distance does have the attractive property that it appears to be independent of overall lesion depth (Groeneveld & Arends, 1975), some aspects of this approach are problematic. First, the sharp interface between sound enamel and air in μCT is often blurred during analysis by attempts to reduce Poisson noise (Gao *et al.*, 1993; Dowker *et al.*, 2003, 2004; Huang *et al.*, 2007). This results in a diffuse interface that spans 3–5 voxels at typical resolutions (Fig. 3*c*). This is further convoluted with the well known partial volume effect (Stock, 2008). Thus, even without the presence of a lesion, the AB distance measurement will be non-zero and one must rely on interpreting partial voxels as sub-voxel lengths. Finally, the coherence of the Advanced Photon Source synchrotron radiation source produces X-ray phase contrast (light and dark fringes) at the interface of materials with different electron density and X-ray absorptivity. These fringes cannot be resolved at the resolution of the present study but can affect LAC values within the boundary voxels. Precise determination of the AB distance is thus quite difficult, especially when the true position of the maximum

falls very close to the enamel surface, as it does in the case of rat lesions. Instead, the AD distance provides a much more robust measure to compare different SZs. This measure includes the entire distance over which the mineral density is greater than the minimum within the lesion, and thus captures the extent to which the SZL differs from an erosive lesion. The AD measure has also been shown to increase with time, as the mineral density minimum decreases in magnitude and moves deeper into the lesion (Theuns *et al.*, 1984; Cochrane *et al.*, 2012), and thus it captures the dynamic nature of lesion progression more accurately.

Most of the SZLs observed here span the majority of the enamel thickness, contrary to observations of WSELs in human enamel (Huang *et al.*, 2007; Cochrane *et al.*, 2012). This may simply result from the combination of much thinner enamel present in the case of rodents and the specific stage of caries observed in this study. If one assumes that the rodent lesion progresses in a similar manner to the human case, the fact that the SZ remains intact in lesions spanning the entirety of the enamel's thickness suggests it is present for the majority of the initial lesion development. This implies that a large amount of mineral must be removed from the lesion, presumably through the intact SZ. As a diffusive barrier, the dynamics of the SZ are thus critical to understanding the overall lesion development. However, the observed demineralization at the DEJ ahead of the lesion presents a possible alternative path for mineral loss, and its potential effects on lesion and SZ progression should not be dismissed. Dissolved mineral could be transported towards the DEJ and removed from the tissue through the pulp cavity *via* the much more porous dentin. While there is currently little evidence to support such a mechanism, its existence would influence the dynamics of SZ formation and would imply significant changes to existing models of early-stage WSEL development.

The value of ρ^*_{max} within the SZ [point B in Fig. 4(*c*)] is never more than 0.52 greater than ρ^*_{min} (point D) in the lesion body. This observation may reflect the fact that continuing demineralization within the lesion body eventually leads to mechanical compromise and lesion collapse, destroying the intact SZ. A similar maximum of $\sim$50% is observed in the average normalized mineral lost values. Future studies incorporating multiple time points and a larger sample size should further explore both of these apparent maxima to provide statistical context for interpreting these observations. If there are true thresholds in these values, it would imply a measureable indicator signalling lesion collapse and would be of interest in studies of lesion formation over time.

Considering the research community's widespread reliance on rodent caries models to explore many aspects of the disease etiology and treatment (Bowen, 2013), it is significant that the present study verifies that the rodent model reproduces the key structural feature of SZs in humans. Furthermore, demonstrating the ability to induce SZLs in a controlled rodent model suggests a potential new tool for investigators specifically looking to study this zone in more detail. While the first direct observation of SZs in rat caries presents an opportunity to begin characterizing and comparing their structure and prevalence to human WSELs, a larger, dedicated animal study with a larger animal count, a consistent cariogenic challenge, and multiple time-points is necessary to firmly establish the prevalence and characteristics of SZs during rat caries.

5. Conclusions

The observations here clearly establish that lesions containing intact SZs can be induced through rodent caries models. A conservative set of criteria applied to depth profiles extracted from three-dimensional μCT data sets has identified 13 clear examples of SZ lesions in M1 molars classified optically to possess moderate caries. These SZs were consistently thinner than those reported in human lesions, irrespective of which previously reported measurement approach was used. The ability to induce SZ lesions in rodents suggests a potentially valuable model system to explore the structure of this crucial zone and deepen our understanding of its role during caries initiation and progression. Furthermore, use of synchrotron μCT provides a means to non-destructively characterize and map SZ lesions with high throughput, enabling the practical execution of large-scale studies with improved statistical relevance. As such, application of the technique will assist efforts to systematically characterize SZ lesions produced within tooth enamel, allowing researchers to begin accounting for the large number of biological, chemical and mechanical variables involved in early caries progression.

Acknowledgements

Research reported in this publication was supported by NIDCR of the National Institutes of Health under award numbers R03DE025303 and R01DE025702. The content is solely the responsibility of the authors and does not necessarily represent the official views of the National Institutes of Health. This work was in part performed at the DuPont-Northwestern-Dow Collaborative Access Team (DND-CAT) located at Sector 5 of the Advanced Photon Source. DND-CAT is supported by Northwestern University, E. I. DuPont de Nemours & Co., and The Dow Chemical Company. This research used resources of the Advanced Photon Source, a US Department of Energy (DOE) Office of Science User Facility operated for the DOE Office of Science by Argonne National Laboratory under Contract No. DE-AC02-06CH11357. This work made use of the OMM Facility supported by the MRSEC program of the National Science Foundation (DMR-1121262) at the Materials Research Center of Northwestern University.

Funding information

The following funding is acknowledged: NIH (award No. R03DE025303; award No. R01DE025702).

References

Al-Jawad, M., Addison, O., Khan, M. A., James, A. & Hendriksz, C. J. (2012). *J. Dent.* **40**, 1074–1080.

Al-Jawad, M., Steuwer, A., Kilcoyne, S. H., Shore, R. C., Cywinski, R. & Wood, D. J. (2007). *Biomaterials*, **28**, 2908–2914.
Arends, J. & Christoffersen, J. (1986). *J. Dent. Res.* **65**, 2–11.
Bowen, W. H. (2013). *Odontology*, **101**, 9–14.
Bowen, W. H., Pearson, S. K., Rosalen, P. L., Miguel, J. C. & Shih, A. Y. (1997). *J. Am. Dent. Assoc.* **128**, 865–871.
CDC (1999). Centers for Disease Control and Prevention, Atlanta, GA, USA.
Cheyne, V. D. (1940). *Exp. Biol. Med.* **43**, 58–61.
Clementino-Luedemann, T. N. R. (2007). PhD thesis, University of Munich (LMU), Germany.
Clementino-Luedemann, T. N. R. & Kunzelmann, K.-H. (2006). *Dent. Mater. J.* **25**, 113–119.
Cochrane, N. J., Anderson, P., Davis, G. R., Adams, G. G., Stacey, M. A. & Reynolds, E. C. (2012). *J. Dent. Res.* **91**, 185–191.
Davis, G. R. & Elliott, J. C. (2006). *Mater. Sci. Technol.* **22**, 1011–1018.
Davis, G. R. & Wong, F. S. L. (1996). *Physiol. Meas.* **17**, 121–146.
Djomehri, S. I., Candell, S., Case, T., Browning, A., Marchall, G. W., Yun, W., Laue, S. H., Webb, S. & Ho, S. P. (2015). *PLoS One*, **10**, e0121611.
Dowker, S. E. P., Dowker, S. E. P., Elliott, J. C., Elliott, J. C., Davis, G. R., Davis, G. R., Wassif, H. S. & Wassif, H. S. (2003). *Caries Res.* **37**, 237–245.
Dowker, S. E. P., Elliott, J. C., Davis, G. R., Wilson, R. M. & Cloetens, P. (2004). *Caries Res.* **38**, 514–522.
Dowker, S. E. P., Elliott, J. C., Davis, G. R., Wilson, R. M. & Cloetens, P. (2006). *Eur. J. Oral Sci.* **114**, 353–359.
Eanes, E. (1979). *J. Dent. Res.* **58**, 829–836.
Elliott, J. C., Dowker, S. E. P. & Knight, R. D. (1981). *J. Microsc.* **123**, 89–92.
Gao, X. J., Elliott, J. C., Anderson, P. & Davis, G. R. (1993). *Faraday Trans.* **89**, 2907–2912.
Gradl, R., Zanette, I., Ruiz-Yaniz, M., Dierolf, M., Rack, A., Zaslansky, P. & Pfeiffer, F. (2016). *PLoS One*, **11**, e0167797.
Groeneveld, A. & Arends, J. (1975). *J. Dent. Res.* **9**, 36–44.
Guvenilir, A., Breunig, T. M., Kinney, J. H. & Stock, S. R. (1997). *Acta Mater.* **45**, 1977–1987.
HHS (2000). US Department of Health and Human Services, National Institute of Dental and Craniofacial Research, National Institutes of Health, Bethesda, MD, USA.
Huang, T. T. Y., He, L. H., Darendeliler, M. A. & Swain, M. V. (2010). *Acta Biomater.* **6**, 4553–4559.
Huang, T. T. Y., Jones, A. S., He, L. H., Darendeliler, M. A. & Swain, M. V. (2007). *J. Dent.* **35**, 737–743.
Kawashita, Y., Kitamura, M. & Saito, T. (2011). *Int. J. Dent.* **2011**, 725320.
Keyes, P. H. (1958). *J. Dent. Res.* **37**, 1088–1099.
Keyes, P. H. (1960). *Arch. Oral Biol.* **1**, 304–320.
Kite, O. W., Shaw, J. H. & Sognnaes, R. F. (1950). *J. Nutr.* **42**, 89–105.
König, K. G., Schmid, P. & Schmid, R. (1968). *Arch. Oral Biol.* **13**, 13–26.
Larson, R. (1981). *Animal Models in Cariology: Proceedings of a Symposium and Workshop on Animal Models in Cariology*, edited by J. M. Tanzer, pp. 195–203.
Lautensack, J., Rack, A., Redenbach, C., Zabler, S., Fischer, H. & Gräber, H.-G. (2013). *Micron*, **44**, 404–409.
Lyngstadaas, S. P., Møinichen, C. B. & Risnes, S. (1998). *Anat. Rec.* **250**, 268–280.
Margolis, H. C., Zhang, Y. P., Lee, C. Y., Kent, R. L. & Moreno, E. C. (1999). *J. Dent. Res.* **78**, 1326–1335.
Nanci, A. (2012). *Ten Cate's Oral Histology: Development, Structure, and Function*, 8th ed. Mosby.
Orland, F. J., Blayney, J. R., Harrison, R. W., Reyniers, J. A., Trexler, P. C., Ervin, R. F., Gordon, H. A. & Wagner, M. (1955). *J. Am. Dent. Assoc.* **50**, 259–272.
Poole, D. F., Mortimer, K. V., Darling, A. I. & Ollis, W. D. (1961). *Nature (London)*, **189**, 998–1000.
Robinson, C., Shore, R. C., Brookes, S. J., Strafford, S., Wood, S. R. & Kirkham, J. (2000). *Crit. Rev. Oral Biol. Med.* **11**, 481–495.
Schaff, F., Bech, M., Zaslansky, P., Jud, C., Liebi, M., Guizar-Sicairos, M. & Pfeiffer, F. (2015). *Nature (London)*, **527**, 353–356.
Schneider, C. A., Rasband, W. S. & Eliceiri, K. W. (2012). *Nat. Methods*, **9**, 671–675.
Shahmoradi, M. & Swain, M. V. (2017). *J. Dent.* **56**, 105–111.
Simmons, L. M., Montgomery, J., Beaumont, J., Davis, G. R. & Al-Jawad, M. (2013). *Arch. Oral Biol.* **58**, 1726–1734.
Stock, S. R. (2008). *Int. Mater. Rev.* **53**, 129–181.
Ten Bosch, J. J. & Angmar-Månsson, B. (1991). *J. Dent. Res.* **70**, 2–14.
Theuns, H. M., van Dijk, J. W. E., Driessens, F. C. M. & Groeneveld, A. (1984). *Caries Res.* **18**, 97–102.
Van Nieuwenhove, V., De Beenhouwer, J., De Carlo, F., Mancini, L., Marone, F. & Sijbers, J. (2015). *Opt. Express*, **23**, 27975–27989.
Vieira, A., Delbem, A. C. B., Sassaki, K. T., Cannon, M. L. & Stock, S. R. (2006). *Proc. SPIE*, **6318**, 631823.
Wefel, J. S. & Harless, J. D. (1984). *J. Dent. Res.* **63**, 1271–1275.
WHO (2012). *Oral health Fact sheet No. 318*, http://www.who.int/mediacentre/factsheets/fs318/en/.
Yamazaki, H., Litman, A. & Margolis, H. C. (2007). *Arch. Oral Biol.* **52**, 110–120.
Yamazaki, H. & Margolis, H. C. (2008). *J. Dent. Res.* **87**, 569–574.
Zanette, I., Enders, B., Dierolf, M., Thibault, P., Gradl, R., Diaz, A., Guizar-Sicairos, M., Menzel, A., Pfeiffer, F. & Zaslansky, P. (2015). *Sci. Rep.* **5**, 9210.